The Astrophysical Journal, 673:647–656, 2008 January 20


# CONFIDENCE LEVEL AND SENSITIVITY LIMITS IN HIGH-CONTRAST IMAGING[1]

Christian Marois,[2] David Lafrenière,[3] Bruce Macintosh,[2] and René Doyon[3]

*Received 2007 June 14; accepted 2007 September 19*


## ABSTRACT

In long adaptive optics corrected exposures, exoplanet detections are currently limited by speckle noise originating from the telescope and instrument optics, and it is expected that such noise will also limit future high-contrast imaging instruments for both ground- and space-based telescopes. Previous theoretical analyses have shown that the time intensity variations of a single speckle follow a modified Rician. It is first demonstrated here that for a circular pupil, this temporal intensity distribution also represents the speckle spatial intensity distribution at a fixed separation from the point-spread function center; this fact is demonstrated using numerical simulations for coronagraphic and noncoronagraphic data. The real statistical distribution of the noise needs to be taken into account explicitly when selecting a detection threshold appropriate for some desired confidence level (CL). In this paper, a technique is described to obtain the pixel intensity distribution of an image and its corresponding CL as a function of the detection threshold. Using numerical simulations, it is shown that in the presence of speckle noise, a detection threshold up to 3 times higher is required to obtain a CL equivalent to that at 5 $\sigma$ for Gaussian noise. The technique is then tested on data acquired by simultaneous spectral differential imaging with TRIDENT and by angular differential imaging with NIRI. It is found that the angular differential imaging technique produces quasi-Gaussian residuals, a remarkable result compared to classical adaptive optic imaging. Finally, a power law is derived to predict the $1 - 3 \times 10^{-7}$ CL detection threshold when averaging a partially correlated non-Gaussian noise.


*Subject headings:* instrumentation: adaptive optics — instrumentation: high angular resolution — methods: data analysis — methods: statistical — planetary systems — stars: imaging — stars: low-mass, brown dwarfs — techniques: image processing

## 1. INTRODUCTION

Searching for faint point sources around bright objects is a challenging endeavor. The atmosphere (Roddier 1981; Racine et al. 1999; Macintosh et al. 2005), telescopes, and instruments optics (Marois et al. 2003, 2005; Hinkley et al. 2007) produce speckles with a range of timescales that limit the direct detection of faint companions. From previous theoretical analyses, it is known that the speckle intensity temporal distribution is a modified Rician (MR; Goodman 1968; Soummer & Aime 2004; Fitzgerald & Graham 2006). If a large number of uncorrelated speckle realizations are co-added, we know from the central limit theorem that the final residual speckle noise will follow a Gaussian intensity distribution. Since atmospheric turbulence produces random speckles that have a very short correlation time, a Gaussian-distributed residual speckle noise is commonly assumed for ground-based adaptive optics (AO) long integrations, and a detection threshold of 5 $\sigma$ is usually considered.

However, careful residual noise analyses of AO images have demonstrated that long exposures are not limited by random, short-lived atmospheric speckles, but by quasi-static speckles (Marois et al. 2003, 2005, 2006; Marois 2004; Masciadri et al. 2005) originating from the telescope and instruments. The speckle noise currently limiting high-contrast ground-based imaging is thus very similar to that limiting space-based observations (Schneider & Silverstone 2003). The typical lifetime of ground-based quasi-static speckles has been found to be from several minutes to hours (Marois et al. 2006; Hinkley et al. 2007); the noise in the combination of several images spanning $\sim$1 hr is very similar to that in a single image (see Fig. 1 for an example acquired with NIRI/Altair at the Gemini telescope). In this case, since the quasi-static speckle noise is well correlated for the entire sequence, the central limit theorem does not apply, and the speckle noise in the final combined image will be non-Gaussian. Sensitivity limits calculated assuming Gaussian statistics would have lower confidence levels (CLs). Finding a robust technique to estimate proper sensitivity limits is fundamental to adequately analyze the sensitivity of an exoplanet survey as a function of angular separation. The contrast limit reached by a survey plays a central role in Monte Carlo simulations used to derive exoplanet frequencies around stars and to constrain planet formation scenarios (Metchev 2006; Carson et al. 2006; Kasper et al. 2007; Lafrenière et al. 2007a). Understanding the residual noise statistical distribution is thus important for future dedicated surveys of next generation AO systems such as NICI (Ftaclas et al. 2003), the Gemini Planet Imager (GPI; Macintosh et al., 2006), and the VLT SPHERE (Dohlen et al. 2006), as well as for future space observatories.

In this paper, a new technique is presented that estimates sensitivity limits of a noise showing arbitrary statistics using a CL approach. The theory behind speckle statistics is summarized in § 2. Then § 3 presents a technique to derive detection thresholds using the probability density function (PDF) and associated CLs.

[1] Based on observations obtained at the Canada-France-Hawaii Telescope (CFHT), which is operated by the National Research Council of Canada, the Institut National des Sciences de l'Univers of the Centre National de la Recherche Scientifique of France, and the University of Hawaii. Also based on observations obtained at the Gemini Observatory, which is operated by the Association of Universities for Research in Astronomy, Inc., under a cooperative agreement with the NSF on behalf of the Gemini partnership: the National Science Foundation (United States), the Particle Physics and Astronomy Research Council (United Kingdom), the National Research Council (Canada), CONICYT (Chile), the Australian Research Council (Australia), CNPq (Brazil), and CONICET (Argentina).

[2] Institute of Geophysics and Planetary Physics L-413, Lawrence Livermore National Laboratory, 7000 East Avenue, Livermore, CA 94550.

[3] Département de Physique and Observatoire du Mont Mégantic, Université de Montréal, C.P. 6128, Succursale Centre-Ville, Montréal, QC H3C 3J7, Canada.

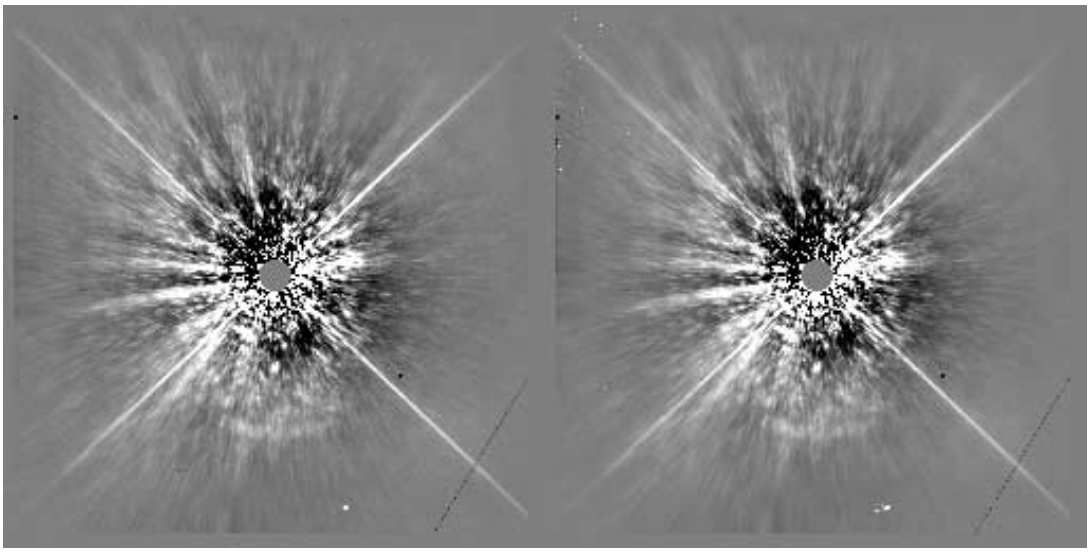

FIG. 1.—Gemini NIRI/Altair quasi-static PSF of the star HD 97334B. A single 30 s exposure is shown (*left*), as well as the median of 90 30 s exposures (*right*). The inner saturated region has been masked. A symmetric radial profile has been subtracted to highlight the speckle noise. The FOV is $20'' \times 20''$. Both images have the same intensity range and linear gray scale.

The technique is applied to simulated (§ 4) and observational (§ 5) data to confirm the theory and to validate the technique. The effect of averaging a sequence of independent non-Gaussian noise realizations is discussed in § 6.1. Concluding remarks follow in § 7.

## 2. SPECKLE NOISE STATISTICS

Following the work of Goodman (1968), Soummer & Aime (2004), and Fitzgerald & Graham (2006), the speckle intensity PDF for one location in the image plane and random temporal phase errors can be shown to be a modified Rician function. At a specific location in the image plane, the MR PDF $p_{\rm MR}(I)$ is a function of the local time-averaged static point-spread function (PSF) intensity $I_c$ and random speckle noise intensities $I_s$:

$$p_{\rm MR}(I) = \frac{1}{I_s} \exp\left(-\frac{I + I_c}{I_s}\right) I_0\left(\frac{2\sqrt{II_c}}{I_s}\right), \qquad (1)$$

where $I$ is the PSF intensity ($I = I_c + I_s$), and $I_0(x)$ is the zero-order modified Bessel function of the first kind. At a specific point of the PSF, if $I_c \gg I_s$, which is relevant to Airy ring pinned speckles, the associated PDF is a Gaussian-like function showing a bright positive tail, while if $I_c \ll I_s$, which is relevant to PSF dark rings or coronagraphic PSFs dominated by second-order halo speckles, the noise distribution is exponential. The CL $\alpha$ for a given detection threshold $d$ is simply obtained by

$$\alpha(d) = \int_{-d}^{d} p'_{\rm MR}(I)\, dI, \qquad (2)$$

where $p'_{\rm MR}$ is the mean-subtracted PDF. Figure 2 illustrates the different possible regimes compared to a Gaussian intensity distribution. For a 5 $\sigma$ detection threshold, where $\sigma$ is the standard deviation of the noise obtained using the `robust_sigma` IDL algorithm,[4] a Gaussian distribution shows a $1 - 3 \times 10^{-7}$ CL,[5] while a MR distribution shows a CL of $\sim 1 - 10^{-2}$ to $1 - 10^{-3}$. The MR distribution is thus producing many more false positive events. For example, consider a survey of many stars in which each observation has a $500 \times 500$ $\lambda/D$ field of view (FOV) (e.g., the $20'' \times 20''$ NIRI/Gemini FOV at $H$-band). If a 5 $\sigma$ detection threshold were selected, the Gaussian noise distribution would lead to 1 false positive detection every 4 stars, while the MR distribution would lead to between ~250 and ~2500 false positives per star. A detection threshold 2–3 times higher is required for the MR distribution to show the same CL as a 5 $\sigma$ Gaussian noise with the same number of false positive events.

In the previous speckle PDF analysis, it was shown that the atmospheric speckle noise PDF is obtained by analyzing the temporal variation at one location of the PSF. For a quasi-static speckle noise, this approach is not adequate, since the noise does not vary significantly with time. The quasi-static noise PDF can be derived using a very simple argument. If we consider a PSF produced by a circular aperture, and if the PDF is obtained by analyzing pixels inside a narrow annulus centered on the PSF core, azimuthal quasi-static speckle noise variations $I_s$ are produced

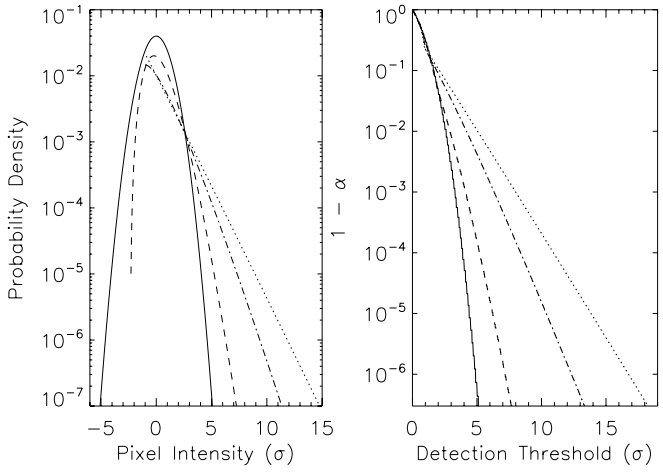


FIG. 2.—*Left*: PDF for a Gaussian distribution (*solid line*) and modified Rician with $I_c/I_s = 10$ (*dashed line*), $I_c/I_s = 1$ (*dot-dashed line*), and $I_c/I_s = 0.1$ (*dotted line*). *Right*: Corresponding CL as a function of detection threshold.

[4] The `robust_sigma` algorithm uses the median absolute deviation as a first estimate of the standard deviation, and then weight points using Tukey's biweight; this algorithm provides another step of robustness to avoid biasing the standard deviation estimate if bad pixels are present.

[5] The expression $1 - 3 \times 10^{-7}$ denotes a CL of 0.9999997. Similar notation is used for CLs throughout the paper.

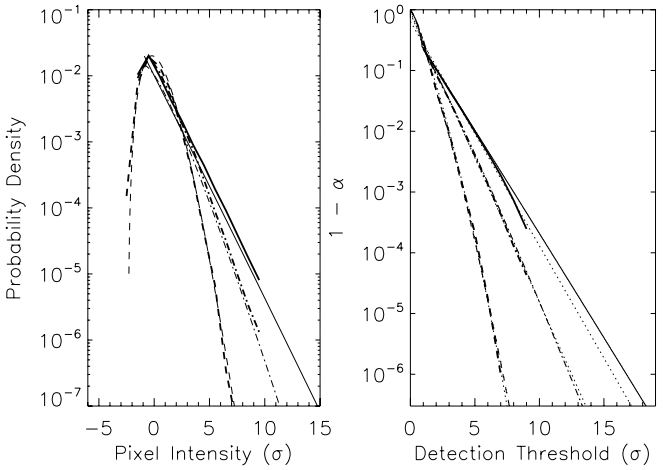


FIG. 3.—PDF (*left*) and CL curves (*right*) obtained from a simulated noise image ($10^6$ resolution elements) generated with an MR intensity distribution compared to the analytical PDF and CL curves. In the left panel, the derived PDFs for $I_c/I_s = 0.1$ (*thick solid line*), $I_c/I_s = 1$ (*thick dot-dashed line*), and $I_c/I_s = 10$ (*thick dashed line*) are shown. The three thin lines are the expected PDFs for the same three cases. The lines in the right panel are the same. The three additional thin dotted lines in the right panel are the extrapolated CL curves.

with the same value of $I_c$ (here, $I_c$ is the unaberrated PSF, and it is azimuthally symmetric for a circular aperture). The speckle noise inside a narrow annulus and from a single speckle noise realization thus shows the same PDF as a temporal speckle noise variation from random phase screens at any location inside the annulus.

## 3. EXPERIMENTAL DERIVATION OF THE PDF AND CL CURVES

A robust technique to derive sensitivity limits can be developed using CLs. The pixel PDF inside a specific region of the image is first obtained, and the CL curve is then derived and extrapolated to estimate a local detection threshold. To avoid having too many false positive detections without missing possible faint companions, a CL of $1 - 3 \times 10^{-7}$ (5 $\sigma$ if Gaussian) is selected here. The basic steps to derive the PDF, to obtain the CL curves, and to estimate the $1 - 3 \times 10^{-7}$ CL detection threshold are summarized as follows.

1. Define an image region.
2. Subtract the mean intensity.
3. Divide the pixel intensities by the noise rms value.
4. Obtain the pixel intensity histogram (PDF).
5. Integrate the PDF between $+d$ and $-d$ to obtain the corresponding CL curve.
6. Perform a polynomial fit on the CL curve.
7. Extrapolate the CL curve to derive the $1 - 3 \times 10^{-7}$ CL detection threshold.

The local PDF is obtained by producing a histogram of the pixel intensities inside a specific region of the image after subtraction of the mean pixel intensity over the region, and division by the noise rms of the image region. The CL curve as a function of detection threshold can be easily estimated by integrating the PDF inside the interval $\pm d$ (see eq. [2]). Due to the limited number of resolution elements (1 $\lambda/D$ for PSFs, or 1 pixel for simulated noise images) in an image, the PDF and CL curves will be known up to a certain detection threshold. In theory, for the $1 - 3 \times 10^{-7}$ CL detection threshold considered here, each area where the PDF needs to be estimated should have several million independent resolution elements. In practice, for images typically containing up to $500 \times 500$ $\lambda/D$ values (250,000 resolution elements), the PDF will be known only up to $\sim 1 - 10^{-5}$ CL for Gaussian noise. A model fit using a $\chi^2$ analysis or a polynomial fit is required to extrapolate the CL curve and obtain the detection threshold corresponding to a $1 - 3 \times 10^{-7}$ CL. Since the CL curves of various distributions are nearly linear in a semi-log $(1 - \alpha)$ versus detection threshold plot (see Fig. 2), we have chosen to use a polynomial fit due to the simplicity of its implementation, its execution speed, and its accuracy. Due to nonlinear effects for detection thresholds near 0 $\sigma$, a linear fit is first performed for detection thresholds above 1.5 $\sigma$. If the detection threshold for a $1 - 3 \times 10^{-7}$ CL is below 9 $\sigma$, a second-order polynomial fit is used instead to better approximate the CL curve for quasi-Gaussian statistics. The CL extrapolation accuracy will be analyzed in the next section.

TABLE 1
CL EXTRAPOLATION ACCURACY FOR SIMULATED STATISTICAL DISTRIBUTIONS

| Statistics | No. Resolution Elements | Expected $d$ ($\sigma$) | $\langle d \rangle$ ($\sigma$) | Standard Deviation ($d$) ($\sigma$) |
|---|---|---|---|---|
| Gaussian ..... | $10^3$ | 5.0 | 5.4 | 1.1 |
| | $10^4$ | | 5.33 | 0.40 |
| | $10^5$ | | 5.06 | 0.29 |
| | $10^6$ | | 5.06 | 0.11 |
| MR10 ..... | $10^3$ | 7.7 | 9.3 | 1.9 |
| | $10^4$ | | 8.20 | 0.95 |
| | $10^5$ | | 8.02 | 0.59 |
| | $10^6$ | | 8.02 | 0.66 |
| MR1 ..... | $10^3$ | 13.5 | 14.9 | 2.5 |
| | $10^4$ | | 13.95 | 0.98 |
| | $10^5$ | | 13.44 | 0.50 |
| | $10^6$ | | 13.48 | 0.37 |
| MR01 ..... | $10^3$ | 18.2 | 18.7 | 2.6 |
| | $10^4$ | | 17.2 | 1.4 |
| | $10^5$ | | 17.13 | 0.40 |
| | $10^6$ | | 17.18 | 0.41 |

NOTES.—The $1 - 3 \times 10^{-7}$ CL detection threshold $d$ is derived by extrapolating different types of MR statistics as a function of the number of resolution elements. MR01 is a modified Rician distribution with $I_c/I_s = 0.1$, while MR1 and MR10 represent $I_c/I_s = 1$ and $I_c/I_s = 10$, respectively. Both the mean and standard deviation of the detection threshold are obtained by analyzing 25 independent noise realizations.

## 4. TECHNIQUE VALIDATION WITH SIMULATED DATA

In this section, the PDF, the CL curve, and the $1 - 3 \times 10^{-7}$ detection threshold of simulated data are obtained.

### 4.1. *Simulated PDFs*

Simulated noise images using specific PDFs are used to test the algorithm's ability to recover the proper $1 - 3 \times 10^{-7}$ detection threshold for known PDFs. To test the effect of the image area size on the CL extrapolation accuracy, images of various sizes are produced following MRs with values of $I_c/I_s$ equal to 0.1, 1, and 10 (see Fig. 2). For each size, 25 independent realizations are computed to derive the extrapolation accuracy. Figure 3 and Table 1 show the CL extrapolation accuracy for simulated statistical distributions. In general, the algorithm slightly underestimates the $1 - 3 \times 10^{-7}$ detection threshold for exponential statistics by $\sim$5%, but usually within the 2 $\sigma$ error calculated for each area size. Typically, the bigger the area is, the more accurate is the detection threshold. To achieve a detection threshold accuracy of 10% for a $1 - 3 \times 10^{-7}$ CL detection threshold, each PDF needs to be known up to a $1 - 10^{-4}$ CL (10,000 resolution

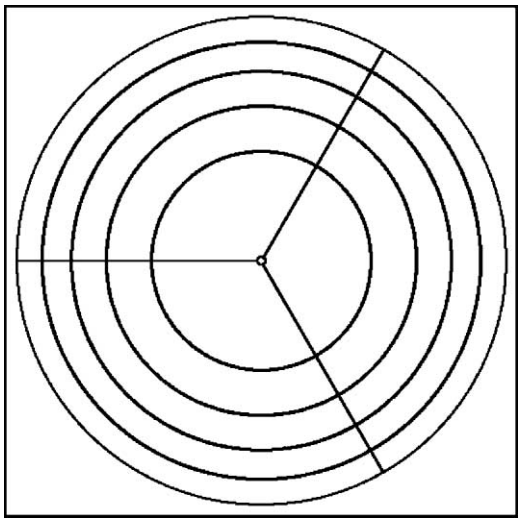

FIG. 4.—Our selected grid for calculating PDFs.

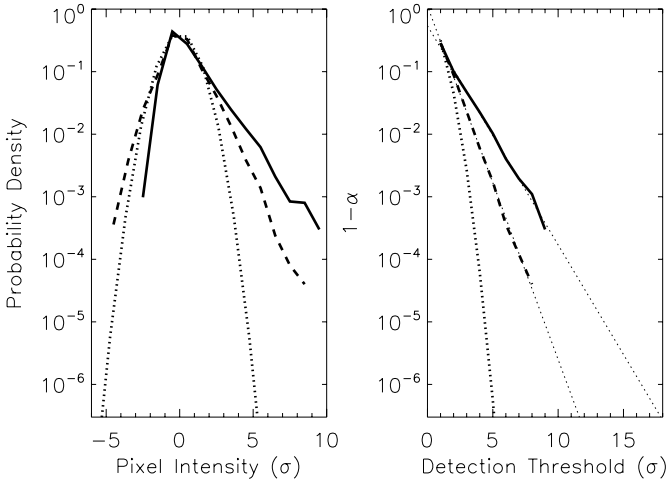


FIG. 5.—PDFs and CLs for simulated PSFs. The dotted line represents a Gaussian noise distribution, while the dashed and solid lines represent simulated aberrated PSFs without and with a Gaussian pupil apodizer, respectively. The right panel shows the corresponding CL, including the power-law fit (*thin dotted lines*) to estimate the $1 - 3 \times 10^{-7}$ CL detection threshold.

elements per area). For instruments with smaller FOVs (several hundred per several hundred $\lambda/D$ values), an area of $\sim 50 \times 50\ \lambda/D$ values (2500 resolution elements) would deliver a detection threshold accuracy of $\sim$15% for all types of distribution. A solution to increase the detection accuracy of small FOVs would be to combine observations of several objects of similar magnitudes and observing conditions in order to increase the number of independent noise realizations in each area.

### 4.2. *Simulated PSFs*

The algorithm is now tested using simulated aberrated PSFs. For PSF observations, determination of the PDF is more complex. The speckle noise amplitude decreases with angular separation, and the PDF may change with angular separation due to the relative importance of random atmospheric speckles, photon, background, and read noises. Since the speckle noise amplitude decreases with angular separation, a signal-to-noise ratio (S/N) image is first obtained by dividing the pixel intensities at each radius by the standard deviation $\sigma$ of the noise at that radius (estimated using the IDL `robust_sigma` algorithm). Finally, since the CLs are extrapolated, a compromise needs to be found between having a good radial sampling of the PDF and having sections of images big enough to adequately determine the PDF.

PSF simulations are performed using fast Fourier transforms (FFTs) of complex $2048 \times 2048$ pixel images with a 512 pixel diameter pupil; the full width at half-maximum (FWHM) of the PSF is 4 pixels. The pupil has uniform amplitude and includes $\lambda/160$ rms of phase errors generated using a power law of index $-2.6$. The PSF images are then trimmed to $1024 \times 1024$ pixels to avoid FFT aliasing effects. An unaberrated reference PSF is subtracted to remove the Airy pattern, and a S/N image is calculated.

For simplicity, consider the calculation of the PDF within an annulus centered on the PSF. Since the presence of background or companion point sources inside that annulus could bias the statistics for real data (we are assuming that the background star density is such that only one or a few background objects are detected in the FOV around any single target; cases with a high background star density will be discussed in section 6.2), we have chosen to divide the annulus into three azimuthal sections containing 50,000 pixels each ($\sim$10,000 resolution elements; see Fig. 4). The median PDF over the three azimuthal sections is calculated. Given the area of these sections, the PDF will be known down to a $\sim 1 - 10^{-4}$ CL for Gaussian statistics, and the $1 - 3 \times 10^{-7}$ detection threshold will be known to $\sim$10% accuracy (see Table 1).

To further avoid cases where a point source is located at the border of two sections, the entire procedure is repeated by rotating the sections by 30° and 60° with respect to the PSF center, and the median PDF over the three orientations is finally obtained. This procedure is repeated at different angular separations.

Since the PDF is estimated in large areas that may contain speckles with $I_c \gg I_s$, $I_c \sim I_s$, or $I_c \ll I_s$, such a technique returns an average PDF weighted by the various speckle noise contributions (pinned/unpinned speckles or Gaussian noises). Simulations with and without a coronagraph (simulated with a Gaussian pupil apodizer having a FWHM equal to one-quarter of the pupil diameter) and for $\lambda/160$, $\lambda/32$, and $\lambda/16$ rms phase aberration are presented (see Figs. 5 and 6). The algorithm clearly detects the MR distribution expected for a pinned speckle-dominated PSF and for an unpinned (exponential) speckle-dominated coronagraphic PSF.

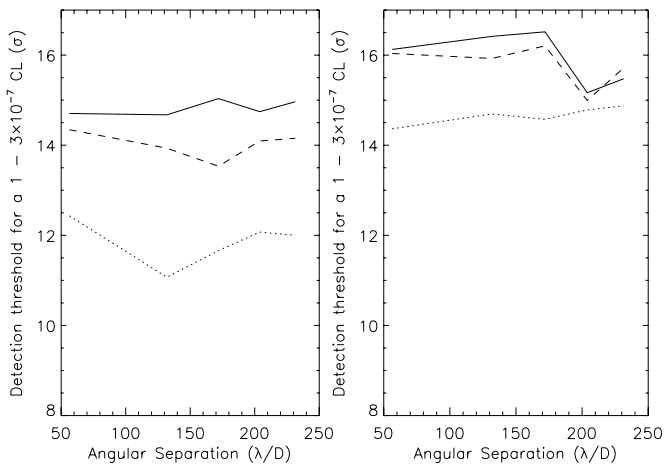


FIG. 6.—Detection threshold required to obtain a $1 - 3 \times 10^{-7}$ CL for simulated aberrated PSFs without (*left*) and with (*right*) a Gaussian pupil apodizer. The solid, dashed, and dotted lines represent $\lambda/16$, $\lambda/32$, and $\lambda/160$ rms values of phase aberration (generated with a power law of index $-2.6$), respectively.

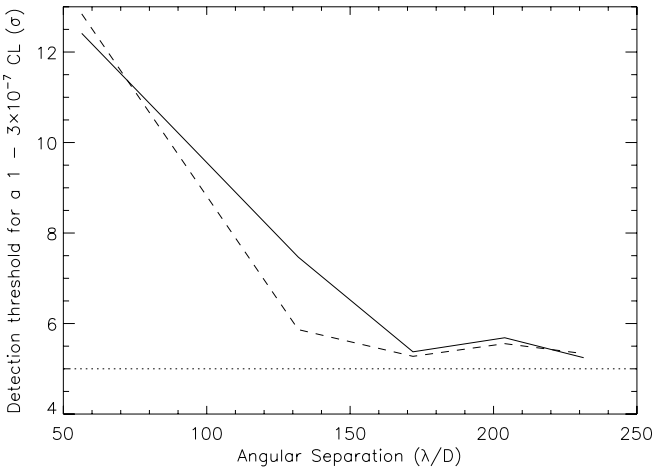


FIG. 7.—See Fig. 6. A random Gaussian pixel-to-pixel noise is added to the PSF image such that it dominates at wide separations.

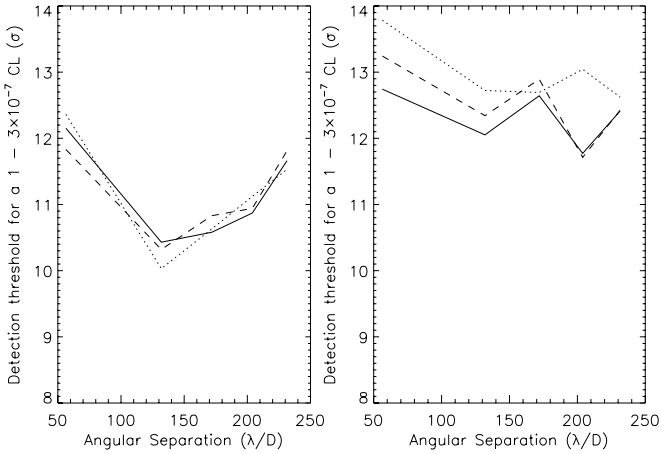


FIG. 8.—See Fig. 6. A partially correlated reference PSF is subtracted (see text for details).

The noncoronagraphic $\lambda/160$ rms simulations confirm that speckle noise follows a MR (with a required detection threshold of $\sim 10\,\sigma$ for a $1 - 3 \times 10^{-7}$ CL), which is expected, since pinned speckles are dominant for this case. As the number of aberrations increases, the ratio of pinned to unpinned speckles decreases, and the noise becomes exponential. For the Gaussian apodized case, since pinned speckles are strongly attenuated, the halo term dominates, and the noise is more exponential. Note that none of these curves are expected to be flat as a function of angular separation, since the ratio of pinned to unpinned speckles varies with angular separation, thus changing the pixel intensity distribution, and some noise is expected from the CL curve extrapolation (see Table 1). Another simulation was performed using the $\lambda/160$ rms case to show that if a constant Gaussian noise (background or read noise) is added to the image, the algorithm correctly detects the change of intensity distribution of the pixels at wide separations (see Fig. 7).

In high-contrast imaging observations, a partially correlated reference star PSF is usually subtracted to remove a fraction of the quasi-static speckle noise. Such reference PSFs can be obtained by observing a nearby target, by acquiring the same star at another wavelength (i.e., simultaneous spectral differential imaging; Marois et al. 2005) or polarization (Potter et al. 2001), or by building the reference using images acquired with different field angles (i.e., angular differential imaging; Marois et al. 2006). Such a PSF subtraction is now simulated to estimate how it affects the PDF. The observed PSF $I$ is simulated with a $\lambda/160$ rms phase aberration $\phi$, with and without a Gaussian apodizer. The reference PSF $I_{\rm ref}$ is constructed by combining a perfectly correlated phase aberration $a\phi$, where $a$ is a constant less than 1, with an uncorrelated part $\Delta\phi$ such as

$$I = \left|\mathrm{FT}\left(Ae^{i\phi}\right)\right|^2, \tag{3}$$

$$I_{\rm ref} = \left|\mathrm{FT}\left(Ae^{i(a\phi+\Delta\phi)}\right)\right|^2, \tag{4}$$

where the total noise rms values of $\phi$ and $a\phi + \Delta\phi$ are equal, and the ratio of the noise rms of $a\phi$ and $\Delta\phi$ is equal to 0.1, 1, and 10. Unless the background, read noise, random atmospheric speckles, or photon noises are achieved by the reference PSF subtraction, the residual PDF is essentially unchanged for cases with and without a coronagraph (see Fig. 8).

## 5. APPLICATION TO OBSERVATIONAL DATA

The steps required to use the algorithm with observational data are similar to the ones described in §§ 3 and 4.2. Only a few additional reduction steps are necessary. Figure 9 illustrates the various steps of the technique using Gemini data.

In addition to the usual data reduction, any deviant pixels, such as might be caused by diffraction from the secondary mirror support, must first be masked. Diffraction from the secondary mirror support usually produces a bright concentrated flux emanating from the PSF core along several azimuthal directions. Since this flux is not produced by quasi-static aberrations and is very localized in the image, they will produce a bright positive tail in the PDF if included, and the $1 - 3 \times 10^{-7}$ CL detection threshold will be overestimated.

Since the main science goal is to detect point sources, noise filtering is also applied to remove noise that is not at the spatial scale of point sources. An $8 \times 8$ FWHM median filter is first subtracted from the image to reject large spatial period noises. Then, a $1 \times 1$ FWHM median filter is applied to reject bad/hot pixels and to smooth out noise with a spatial period below the resolution limit. The image is finally divided at each radius by the standard deviation $\sigma$ of the noise (again obtained with the IDL `robust_sigma` algorithm) to obtain a S/N image.

The algorithm is first tested using data obtained at the Gemini telescope with the Altair adaptive optics system (Saddlemyer et al. 1998) and the NIRI near-infrared camera (Hodapp et al. 2000). These data are part of the Gemini Deep Planet Survey (Lafrenière et al. 2007a), which uses the angular differential imaging (ADI) technique (Marois et al. 2006; Lafrenière et al. 2007b) to detect faint companions. This technique consists of acquiring a sequence of images with continuous FOV rotation. A reference PSF that does not contain any point sources is first obtained by combining images of the sequence, and the quasi-static speckle noise is then attenuated by subtracting the reference ADI PSF. The data for the star HD 97334B (program GN-2005A-Q16), acquired on 2005 April 18 with good seeing conditions (Strehl ratio of 0.2 at $H$-band), are presented. These data have been reduced, registered, and processed using the pipeline described in Marois et al. (2006), with the additional steps mentioned above, i.e., pixel masking, noise filtering, and normalizing. Given that NIRI images are $1024 \times 1024$ pixels, and that PSFs have 3 pixels per FWHM, we have chosen the same areas as the simulated PSFs mentioned above (see § 4.2) to calculate the PDF. For each region of the image, the pixel intensity histogram is obtained and integrated to derive the CL curve. The CL is then extrapolated using a polynomial fit, and the $1 - 3 \times 10^{-7}$ CL detection threshold is estimated. The derived detection thresholds for a $1 - 3 \times 10^{-7}$ CL are presented

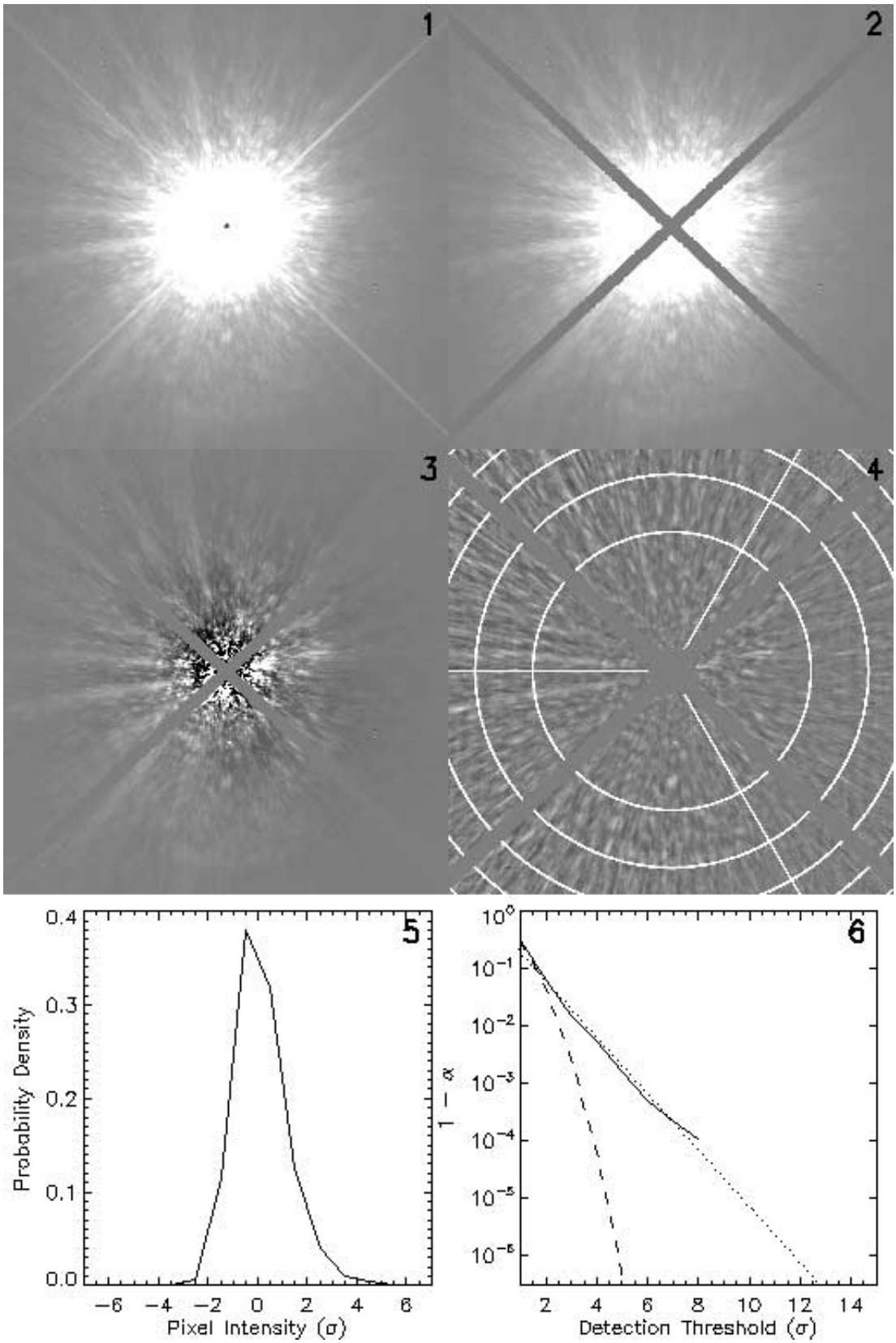


FIG. 9.—Different steps involved in estimating a detection threshold in a specific region of the PSF using the CL approach. Panel 1 shows a Gemini CH4-short saturated PSF image that has been reduced and registered to the image center. Panels 2, 3, and 4 show the same PSF image, but with the secondary support structure diffraction masked, after noise filtering, and after noise normalizing, respectively. Panels 5 and 6 show respectively the pixel intensity distribution (PDF) and corresponding CL curve inside a typical region of the PSF shown in panel 4. An extrapolation of the CL curve gives the $1 - 3 \times 10^{-7}$ CL detection threshold for that region (here approximately 12.6 $\sigma$). Steps illustrated by panels 5 and 6 are repeated for all regions of the PSF, and after rotating the regions by 30° and 60° to eliminate the bias resulting from point sources located at the edge of two regions.

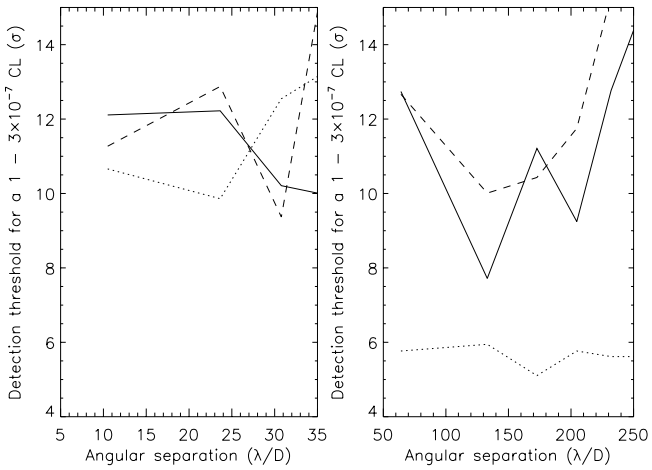


FIG. 10.—*Left*: TRIDENT SSDI–required detection threshold for a $1 - 3 \times 10^{-7}$ CL of the star $\upsilon$ And acquired at the Canada-France-Hawaii telescope. Solid, dashed, and dotted lines show the required detection limit for the TRIDENT PSF, the SSDI simple difference subtraction (a subtraction of two images acquired simultaneously at two wavelengths), and the SSDI simple difference minus the reference SSDI simple difference image of a reference star, respectively. *Right*: Same plot, but for the ADI technique and the star HD 97334B acquired at Gemini. Solid, dashed, and dotted lines represent a single PSF image minus a symmetric radial profile (spiders masked), a single ADI reference–subtracted image, and the total ADI median combined image (the median of 90 ADI-subtracted images), respectively.

(see Fig. 10) for a single PSF, a PSF minus the ADI reference PSF, and the combined ADI-subtracted images.

The algorithm is next tested using observational data obtained at the Canada-France-Hawaii telescope using the PUEO adaptive optics system (Rigaut et al. 1998) and the TRIDENT near-infrared camera (Marois et al. 2005). TRIDENT is a triple-beam multiwavelength (1.58, 1.625, and 1.68 $\mu$m with 1% bandpass) imager built following the simultaneous spectral differential imaging technique (Racine et al. 1999; Marois et al. 2000). The technique consists of acquiring several images at different wavelengths and subtracting them to attenuate the speckle noise, while retaining most of the flux of nearby companions. These data have been acquired as part of a direct imaging survey of stars confirmed to possess exoplanets from radial velocity analysis. The data set of the star $\upsilon$ And, acquired on 2002 November 14, is used here. Seeing conditions were relatively good, and the Strehl ratio was on the order of 0.5. The data have been reduced by subtracting a dark image, dividing by a flat field, correcting for bad/hot pixels, and registering the PSF at the image center. An optimized reference PSF is obtained using a star ($\chi$ And) with a similar spectral type and magnitude, and which was acquired at the same decl. and h.a. to minimize the PSF's evolution from differential atmospheric refraction and flexure effects. Performances with and without the simultaneous reference PSF and the $\chi$ And reference PSF subtractions are analyzed. Due to the limited FOV of TRIDENT, sections of 10,000 pixels (500 resolution elements, given that TRIDENT has 5 pixels per $\lambda/D$) are used to derive the PDF. Detection thresholds are thus known to ~15% (see Table 1).

It is clear that raw PSFs from both TRIDENT and Gemini are limited by a non-Gaussian noise. For both TRIDENT/CFHT and NIRI/Gemini images, even after subtraction of a reference PSF, the residuals are still dominated by quasi-static speckles rather than averaged atmospheric speckle, background, read, or photon noises. Only the final combined ADI-subtracted image possesses a clear Gaussian-like noise. Figure 11 shows a visual example of a 5 $\sigma$ detection both with and without a Gaussian-distributed noise after introducing artificial 5 $\sigma$ point sources. For the Gaussian-distributed noise, only those artificial point sources with a detection threshold at 5 $\sigma$ are detected,[6] while for the Gemini data (a MR-distributed noise), numerous false positive sources are observed for the same detection threshold. If we instead select the $1 - 3 \times 10^{-7}$ CL detection threshold obtained by the technique described in this paper (here equal to 10 $\sigma$; see Fig. 10), then only the artificial point sources are detected. It is interesting to note that the artificial source detection CLs in the left and right panels of Figure 11 are the same.

## 6. DISCUSSIONS

### 6.1. *PDF Evolution with Quasi-static Speckle Averaging*

It was shown in § 5 that the ADI technique produces a quasi-Gaussian noise. This is mainly due to the FOV rotation that occurs during the observing sequence; the residual noise is averaged incoherently when combining the images after FOV alignment. From the central limit theorem, it is thus expected that the noise in the final combined image shows quasi-Gaussian statistics.

In this section, simulations are presented that estimate the number of independent speckle noise realizations required to converge to a quasi-Gaussian noise intensity distribution. Random noise images with $10^6$ resolution elements are created following an MR distribution with $I_c/I_s$ values equal to 0.1, 1, and 10. The PDF and CL curves are calculated for a single realization up to the co-addition of 25 independent realizations (see Fig. 12). Typically, ~20 independent realizations are required for the MR distribution to be equal to a Gaussian distribution to within ~20%. Figure 13 shows the detection threshold $d$ for a $1 - 3 \times 10^{-7}$ CL as a function of $n_{\rm eff}$, the number of independent noise realizations:

$$n_{\rm eff} = n \frac{t_{\rm exp}}{\tau_{\rm dcorr}}, \tag{5}$$

where $n$ is the number of acquired images in the sequence, $t_{\rm exp}$ is the integration time per image, and $\tau_{\rm dcorr}$ is the speckle noise decorrelation timescale (the equation is valid if $\tau_{\rm dcorr} \geq t_{\rm exp}$; if $\tau_{\rm dcorr} < t_{\rm exp}$ then $n_{\rm eff} = n$). These three curves can be well fit by a simple power law of the form

$$d(n) = (d_1 - 5) n_{\rm eff}^{-0.63} + 5, \tag{6}$$

where $d_1$ is the detection threshold of a single image for a $1 - 3 \times 10^{-7}$ CL. This equation is valid for all types of statistical distributions studied here. Equation (6) can be used to predict the detection threshold required for a $1 - 3 \times 10^{-7}$ CL and a statistical distribution with a known instantaneous PDF and speckle noise decorrelation timescale. If we consider the Gemini ADI observation ($d_1 \sim 13$ for a single ADI-subtracted image; see Fig. 10), for a 70 minute observation sequence with $\tau_{\rm dcorr} \sim$ 1.5 minutes (at 2″ or 50 $\lambda/D$; see Marois et al. 2006), it is expected that the detection threshold for a $1 - 3 \times 10^{-7}$ CL of the final combined image ($n_{\rm eff} = 46.7$) will be ~5.7 at 50 $\lambda/D$, which is in good agreement with the number derived with real images (~5.8; see Fig. 10).

[6] Only approximately half of the artificial point sources are detected ≥5 $\sigma$, since the artificial sources, being 5 $\sigma$ in intensity, vary in S/N by 1 $\sigma$ rms due to the underlying noise in the image. A 5 $\sigma$ detection threshold thus misses/detects ~50% of 5 $\sigma$ sources.

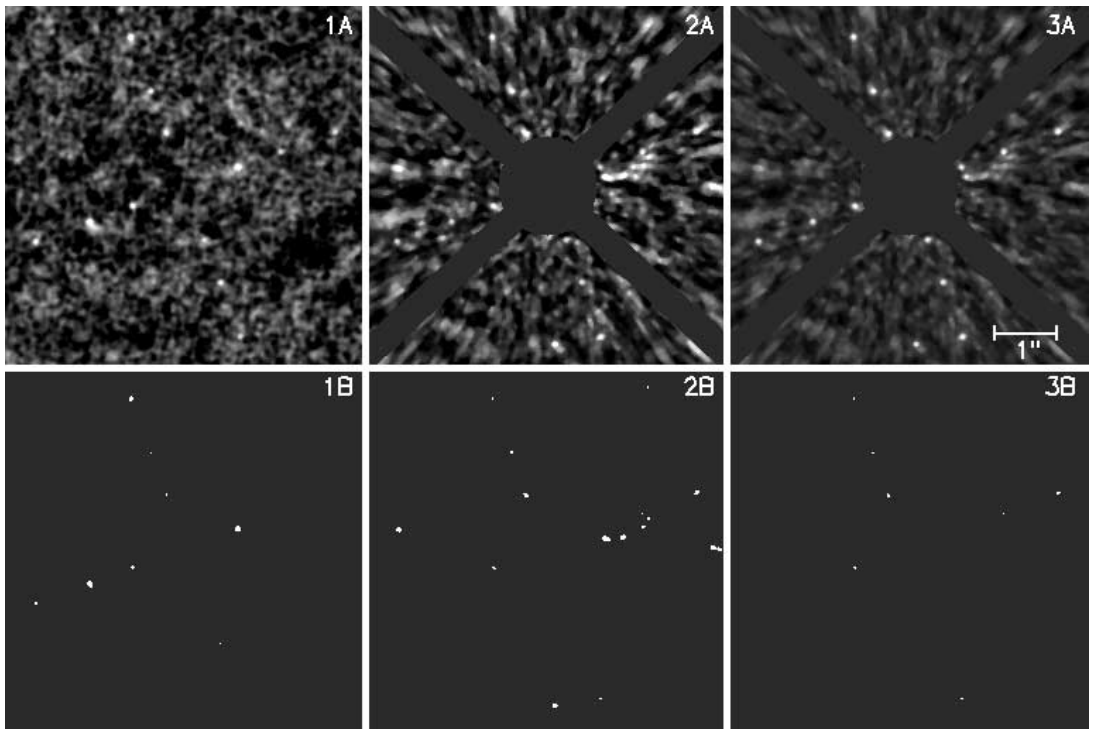


FIG. 11.—Images of $1 - 3 \times 10^{-7}$ CL detections for a Gaussian-distributed noise and Gemini data. After analyzing the noise statistical distribution, artificial point sources are added at $0.9''$, $1.6''$, and $2.5''$ from the image center at P.A. values of $20^\circ$, $110^\circ$, $200^\circ$, and $290^\circ$ from the vertical axis, each with an intensity equal to 5 $\sigma$ of the noise. Panel 1A shows the image generated using a Gaussian noise (a display with a linear intensity range between $-1$ and 5 $\sigma$). Panel 1B shows the pixels that are higher than 5 $\sigma$. Panels 2A and 2B are similar, but represent the Gemini PSF. Panels 3A and 3B are again similar, but represent artificial point sources that now have an intensity equal to 10 $\sigma$ of the noise, the detection threshold derived using the CL technique. The FOV is $5.65'' \times 5.65''$. Panel 3A is displayed with a linear intensity range between $-2$ and 10 $\sigma$.

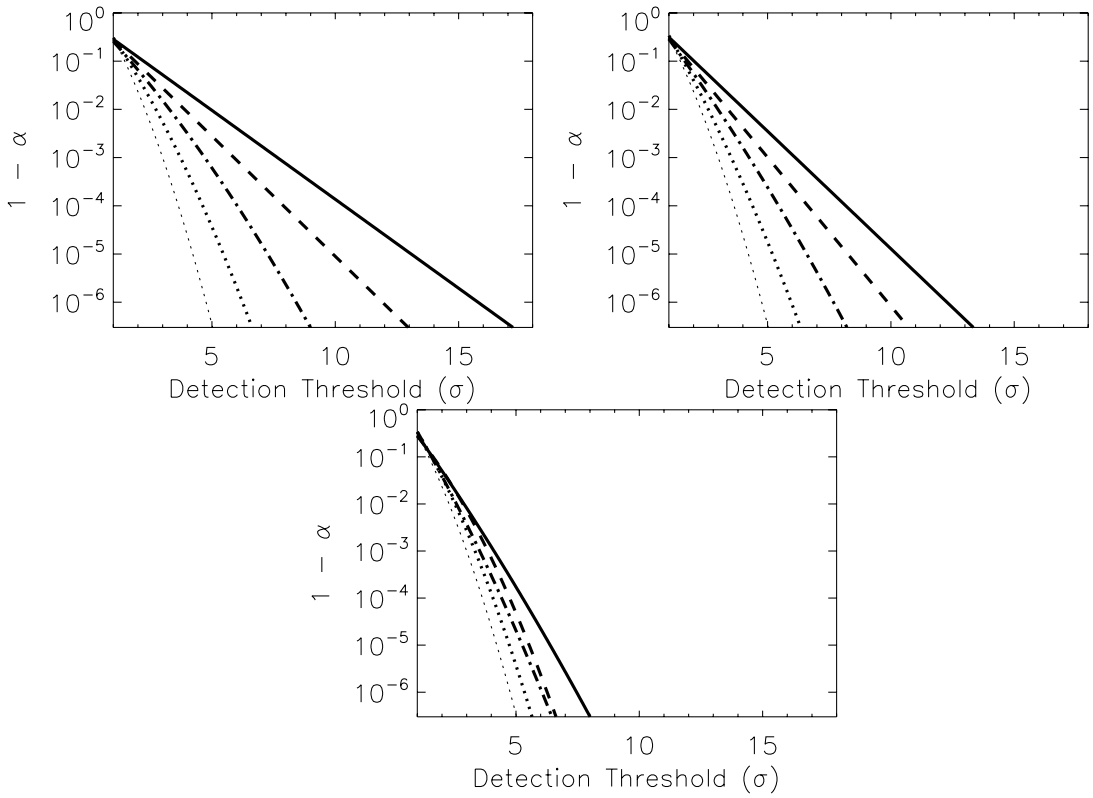


FIG. 12.—Extrapolated CL curves (from $10^6$ resolution element simulations) as functions of the detection threshold for various values of $n_{\rm eff}$. The upper left panel represents an MR statistical distribution with $I_c/I_s = 0.1$, while the upper right and bottom panels represent $I_c/I_s = 1$ and $I_c/I_s = 10$, respectively. The thick solid line represents a single noise realization, while the thick dashed, thick dot-dashed, and thick dotted lines represent the average of 2, 5, and 25 independent noise realizations, respectively. The thin dotted line represents the CL curve for a Gaussian noise intensity distribution.

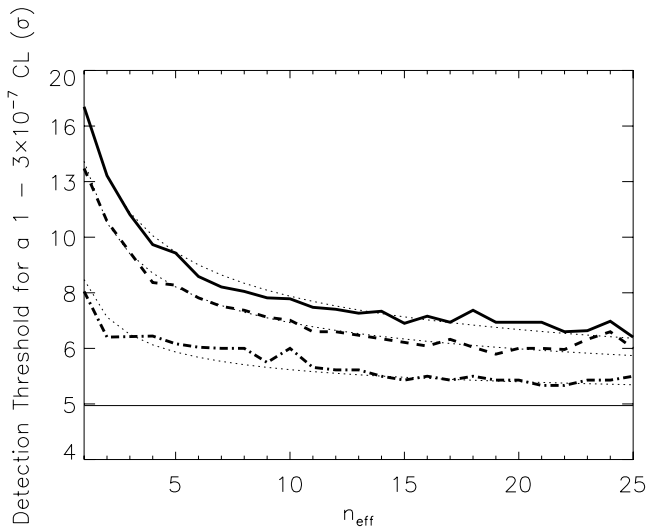


FIG. 13.—The $1 - 3 \times 10^{-7}$ CL detection threshold as a function of $n_{\rm eff}$, the number of independent noise realizations. The thick line represents an MR statistical distribution with $I_c/I_s = 0.1$, while the thick dashed and thick dot-dashed lines represent $I_c/I_s = 1$ and $I_c/I_s = 10$, respectively. The thin solid line represents Gaussian statistics. The three thin dotted lines are the predicted detection thresholds derived from the fitted power law (see text for details).

### 6.2. *Targets with a High Background Star Density*

In some cases, it is desirable to observe an interesting nearby target situated along the Galactic plane or in front of the Galactic bulge. In those areas, the high background stellar density implies that numerous background stars will be present in each of the areas defined, allowing us to derive pixel intensity distributions. The detection threshold obtained will be affected by those stars, since the algorithm would consider them as speckles. Several techniques can be used to remove the stars before estimating detection thresholds. A simple solution is to subtract these stars, using a nonsaturated image of the primary, and mask any remaining contaminated areas with a not-a-number (NaN) mask. If the observations are obtained using the ADI technique, then a star-free residual image can be obtained in the following manner. Prior to combining all the ADI-subtracted images together, instead of rotating them by the angle required to align their field of view, they are rotated by the negative of that angle such that all off-axis sources (the background stars) are eliminated by the median combination. As the amplitude of the rotation between the images is the same as for the "proper" combination, the effect of the median combination on the residual noise is expected to be the same, and this star-free residual image can be used to estimate the noise distribution. Of course, the proper ADI combination of images must be used to search for companions. Another approach, still within the ADI framework, is to use the final ADI residual image to subtract the off-axis sources from each nonrotated ADI-subtracted image. These source-free images are then rotated by the negative of the angle needed to align their fields of view, such that their median combination eliminates the off-axis sources subtraction residuals. As in the previous technique, this source-free residual image should have the same residual noise distribution as the proper ADI residual image.

## 7. CONCLUSION

A robust technique has been elaborated to estimate sensitivity limits using a CL approach. This technique correctly finds the expected MR intensity distributions of simulated and real PSFs, and properly detects a change of PDF as a function of angular separation. Experiments with simulated and observational data confirm the prediction of the theory that raw PSFs obtained with high-contrast imaging instruments are limited by a non-Gaussian noise. A correction factor (up to 3) needs to be applied to detection limits calculated assuming Gaussian statistics in order to obtain the desired $1 - 3 \times 10^{-7}$ CL detection threshold. Properly estimating this effect is important for future high-contrast imaging instruments for both ground- and space-based dedicated missions, since a loss of a factor of 3 in contrast results in less sensitivity to low-mass exoplanets; alternatively, if a specific contrast needs to be achieved, integration times need to be at least 9 times longer. It has been shown that the ADI technique is the only observing strategy currently known that intrinsically generates a quasi-Gaussian noise at all separations where sufficient FOV rotation has occurred. A simulation has shown that it typically takes $\sim$20 independent speckle noise realizations to produce an average speckle noise that shows quasi-Gaussian statistics. A general power law has been derived to predict the detection threshold required when averaging independent speckle noise realizations of known PDFs and decorrelation timescales.

The authors would like to thank Rémi Soummer, Mike Fitzgerald, James Graham, Anand Sivaramakrisnan, Lisa Poyneer, and Daniel Nadeau for discussions. This research was performed under the auspices of the US Department of Energy by the University of California Lawrence Livermore National Laboratory under contract W-7405-ENG-48, and also supported in part by the National Science Foundation Science and Technology Center for Adaptive Optics, managed by the University of California at Santa Cruz under cooperative agreement AST 98-76783. This work is also supported in part through grants from the Natural Sciences and Engineering Research Council, Canada, and from the Fonds Québécois de la Recherche sur la Nature et les Technologies, Québec.

## REFERENCES

Carson, J. C., Eikenberry, S. S., Smith, J. J., & Cordes, J. M. 2006, AJ, 132, 1146
Dohlen, K., et al. 2006, SPIE, 6269, 24
Fitzgerald, M. P., & Graham, J. R. 2006, ApJ, 637, 541
Ftaclas, C., Martín, E. L., & Toomey, D. 2003, in IAU Symp. 211, Brown Dwarfs, ed. Eduardo Martín (San Francisco: ASP), 521
Goodman, J. W. 1968, Introduction to Fourier Optics (San Francisco: McGraw Hill)
Hinkley, S., et al. 2007, ApJ, 654, 633
Hodapp, K., Hora, J., Graves, E., Irwin, E. M., Yamada, H., Douglass, J. W., Young, T. T., & Robertson, L. 2000, Proc. SPIE, 4008, 1334
Kasper, M., Apai, D., Janson, M., & Brandner, W. 2007, A&A, 472, 321
Lafrenière, D., Marois, C., Doyon, R., Nadeau, D., & Artigau, É. 2007b, ApJ, 660, 770
Lafrenière, D., et al. 2007a, ApJ, 670, 1367
Macintosh, B., Poyneer, L., Sivaramakrishnan, A., & Marois, C. 2005, Proc. SPIE, 5903, 170
Macintosh, B., et al. 2006, SPIE, 6272, 20
Marois, C. 2004, PhD. thesis, Université de Montréal
Marois, C., Doyon, R., Nadeau, D., Racine, R., & Walker, G. A. H. 2003, in Astronomy with High Contrast Imaging: From Planetary Systems to Active Galactic Nuclei, ed. C. Aime & S. Soummer (Les Ulis: EDP), 233
Marois, C., Doyon, R., Racine, R., & Nadeau, D. 2000, PASP, 112, 91
Marois, C., Doyon, R., Racine, R., Nadeau, D., Riopel, M., Vallée, P., & Lafrenière, D. 2005, PASP, 117, 745
Marois, C., Lafrenière, D., Doyon, R., Macintosh, B., & Nadeau, D. 2006, ApJ, 641, 556
Masciadri, E., Mundt, R., Henning, Th., Alvarez, C., & Barrado y Navascués, D. 2005, ApJ, 625, 1004

Metchev, S. A. 2006, Ph.D. thesis, California Institute of Technology
Potter, D., Baudoz, P., Guyon, O., Brandner, W., Close, L., Graves, J. E., & Northcott, M. 2001, BAAS, 33, 812
Racine, R., Walker, G. A. H., Nadeau, D., Doyon, R., & Marois, C. 1999, PASP, 111, 587
Rigaut, F., et al. 1998, PASP, 110, 152
Roddier, F. 1981, Progress in Optics, 19, 281
Saddlemyer, L. K., Herriot, G., Veran, J.-P., & Fletcher, J. M. 1998, Proc. SPIE, 3353, 150
Schneider, G., & Silverstone, M. D. 2003, Proc. SPIE, 4860, 1
Soummer, R., & Aime, C. 2004, SPIE, 5490, 495